Stress-strain response of hydrate-bearing sands: Numerical study using discrete element method simulations

Jong-Won Jung,[1] J. Carlos Santamarina,[2] and K. Soga[3]

Received 16 November 2011; revised 20 February 2012; accepted 22 February 2012; published 27 April 2012.

[1] Gas hydrate is a crystalline solid found within marine and subpermafrost sediments. While the presence of hydrates can have a profound effect on sediment properties, the stress-strain behavior of hydrate-bearing sediments is poorly understood due to inherent limitations in laboratory testing. In this study, we use numerical simulations to improve our understanding of the mechanical behavior of hydrate-bearing sands. The hydrate mass is simulated as either small randomly distributed bonded grains or as "ripened hydrate" forming patchy saturation, whereby sediment clusters with 100% pore-filled hydrate saturation are distributed within a hydrate-free sediment. Simulation results reveal that reduced sand porosity and higher hydrate saturation cause an increase in stiffness, strength, and dilative tendency, and the critical state line shifts toward higher void ratio and higher shear strength. In particular, the critical state friction angle increases in sands with patchy saturation, while the apparent cohesion is affected the most when the hydrate mass is distributed in pores. Sediments with patchy hydrate distribution exhibit a slightly lower strength than sediments with randomly distributed hydrate. Finally, hydrate dissociation under drained conditions leads to volume contraction and/or stress relaxation, and pronounced shear strains can develop if the hydrate-bearing sand is subjected to deviatoric loading during dissociation.

Citation: Jung, J.-W., J. C. Santamarina, and K. Soga (2012), Stress-strain response of hydrate-bearing sands: Numerical study using discrete element method simulations, *J. Geophys. Res.*, *117*, B04202, doi:10.1029/2011JB009040.

1. Introduction

[2] Gas hydrates are crystalline solids found in marine and permafrost sediments. The stiffness, strength and volume change behavior of hydrate-bearing sediments are important parameters for the analysis of well stability [*Klar et al.*, 2010; *Masui et al.*, 2005a; *Rutqvist and Moridis*, 2009], seafloor stability [*Nixon and Grozic*, 2007], and reservoir simulations in view of production strategies [*Moridis et al.*, 2011].

[3] Triaxial compression, direct shear strength and bending tests have been used to study the mechanical properties of hydrate-bearing sediments [*Ebinuma et al.*, 2005; *Hyodo et al.*, 2008; *Masui et al.*, 2005b; *Ohmura et al.*, 2002; *Yun et al.*, 2007]. Published data suggest that the stiffness, strength and the dilative tendency of hydrate-bearing sediments increase with hydrate saturation and are affected by hydrate formation history, initial confining stress, and temperature [*Ebinuma et al.*, 2005; *Hyodo et al.*, 2008; *Ohmura et al.*, 2002; *Yun et al.*, 2007] (see reviews by *Soga et al.* [2006] and *Waite et al.* [2009]). In particular, the stress-strain response of hydrate-bearing sediments is affected by pore habit; for example, hydrate formation at interparticle contacts causes a greater increase in strength and stiffness than pore-filling hydrate [*Waite et al.*, 2009]. However, difficulties in controlling hydrate formation, distribution, saturation, and pore habit challenge the interpretation of laboratory studies.

[4] In this manuscript, we use the discrete element method (DEM) to model hydrate-bearing sands to understand their stress-strain response and to gain insight into underlying particle level processes. We explore the effects of hydrate distribution, saturation, sediment porosity, confining stress, and pore habit.

2. Numerical Simulation

[5] We use the commercially available discrete element code Particle Flow Code in Three Dimensions v3.10 (PFC3D). The simulated specimen preparation and other model details follow.

2.1. Specimen Preparation

[6] Sand specimens are formed within a stress-controlled cylindrical volume (diameter = 10 mm, height = 20 mm). Small mineral grains, half their target size, are randomly placed within the cylindrical volume. Gradually, the mineral grains are enlarged at a rate of $\Delta R/R_o = 0.0005$ per cycle; the system is allowed to equilibrate with the boundary forces in every cycle (i.e., each cycle ends without particle

[1]Lawrence Berkeley National Laboratory, Berkeley, California, USA.
[2]School of Civil and Environmental Engineering, Georgia Institute of Technology, Atlanta, Georgia, USA.
[3]Department of Engineering, University of Cambridge, Cambridge, UK.

0148-0227/12/2011JB009040

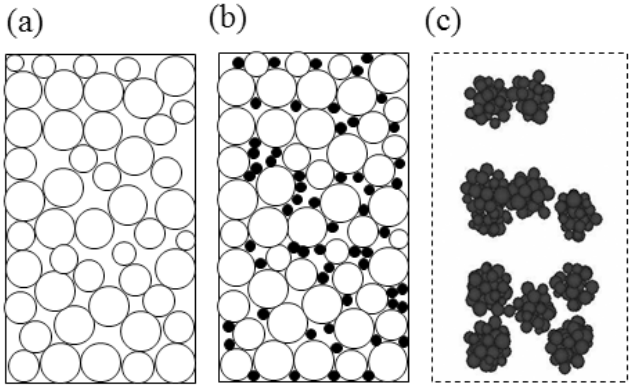

Figure 1. Simulation of hydrate-bearing sediments. (a) Hydrate-free sediments. (b) Distributed hydrate. (c) Patchy hydrate saturation: the grain clusters are shown in 3D (all other particles are transparent). Clusters have 100% hydrate saturation, while the sediment matrix has no hydrate.

overlapping). This "grain growth and equilibration" cycle is repeated about 1500 times until the target diameter is reached; this is the initial hydrate-free sediment packing (Gaussian diameter distribution between 0.62 mm to 0.82 mm; Figure 1a). The hydrate-free sediment is then subjected to isotropic confinement (σ'_o = 0.1 MPa to 1 MPa). Two values of initial porosity before confinement are generated to simulate both loose n = 0.532 (3,762 particles) and dense n = 0.402 (4,806 particles) sediments.

[7] We explore two different hydrate pore habits. "Distributed hydrate" reflects recent heterogeneous nucleation; it is simulated with small hydrate particles that randomly bond onto mineral grains (similar to studies of cemented soil by *Wang and Leung* [2008]). Hydrate particles are randomly placed within the sediment pores after consolidation to the predetermined isotropic stress σ'_o (Figure 1b). Initially, hydrate particles are one tenth the target size; then, they are gradually enlarged to the target diameter of 0.22 mm which is about 1/3 the diameter of the mineral particles. Finally, hydrate particles are randomly moved in different directions until they attach onto mineral surfaces or other hydrate particles. Hydrate particles may come into contact with other surfaces during shear and volume change. The parallel bond model in PFC3D is used to impose the bonding strength between hydrate and mineral particles. Bonding strength and stiffness are obtained from experimental results (Table 1) [*Jung and Santamarina*, 2011]. The number of hydrate particles added to the sediment is used to control the hydrate saturation S_h between 0 and 50%. The total number of hydrate particles reaches 74,940 for a hydrate saturation S_h = 50% in sediments with initial porosity n = 0.532.

[8] The second pore habit "patchy saturation" reflects ripened hydrate; it is simulated as clusters of mineral grains with 100% hydrate saturation (bonded mineral particles), inside a hydrate-free sediment mass (Figure 1c). Each sand cluster consists of 15–30 mineral grains. Cluster size and the number of clusters determine the global hydrate saturation (between S_h = 0 and 50%). Mineral grains that are part of a cluster are parallel bonded together after the sediment has been consolidated to the predetermined isotropic stress σ'_o. A high bonding strength of 20 MPa is used to prevent cluster breakage during deviatoric loading.

[9] All other simulation parameters are the same in both cases: normal contact stiffness 1×10^7 [N/m], shear stiffness 1×10^7 [N/m], interparticle friction coefficient μ = 0.5, and specific gravity Gs = 2.65.

2.2. Triaxial Compression Test Simulation

[10] The top and bottom caps are modeled as rigid frictionless plates. Axial deviatoric loading is applied while keeping a constant confining pressure σ_c on the cylindrical wall. We simulate tests for various initial sediment porosities, hydrate saturations, and confining stresses for the two different hydrate pore habits.

3. Numerical Results

[11] The porosity after isotropic consolidation to 1 MPa is n = 0.361 for the dense sand and n = 0.393 for loose sand (note initial porosities before consolidation are n = 0.402 and 0.532, respectively). The deviatoric stress, and both axial and volumetric strains are recorded during deviatoric loading and dissociation tests. In addition, particle-scale information is stored for post processing. Parameters used to report and analyze the data are defined first.

3.1. Data Reporting and Analysis: Parameters and Definitions

[12] The sediment responds to effective stresses σ'_1, σ'_2 and σ'_3. In axial-compression triaxial tests, the cylindrical specimen is subjected to confining stress $\sigma'_o = \sigma'_2 = \sigma'_3$, and the principal stress σ'_1 combines the confining stress and the deviatoric stress applied with the vertical shaft. Let's define the mean effective stress $p' = (\sigma'_1 + \sigma'_2 + \sigma'_3)/3$ and the deviatoric stress $q = (\sigma'_1 - \sigma'_3)$.

Table 1. Material Properties

Parameter	Value
Soil Particles	
Soil particle density (kg/m^3)	2650
Initial porosity (before consolidation)	0.402 and 0.532
Particle radii range (m)	0.62×10^{-3}-to-0.82×10^{-3}
Interparticle friction coefficient	0.5
Normal contact stiffness (N/m)	1×10^7
Shear contact stiffness (N/m)	1×10^7
Distributed Hydrate	
Hydrate particle density (kg/m^3)	2650
Hydrate particle radius (m)	0.22×10^{-3}
Assumed bond radius (m)	0.22×10^{-3}
Normal contact stiffness (N/m)	1.54×10^8
Shear contact stiffness (N/m)	1.54×10^8
Hydrate-mineral normal bonding strength (N/m^2)	2×10^5
Hydrate-mineral shear bonding strength (N/m^2)	2×10^5
Patchy Hydrate Saturation	
Soil particle density (kg/m^3)	2650
Particle radii ranges (m)	0.62×10^{-3}-to-0.82×10^{-3}
Interparticle friction coefficient	0.5
Normal bonding strength (N/m^2)	2×10^7
Shear bonding strength (N/m^2)	2×10^7

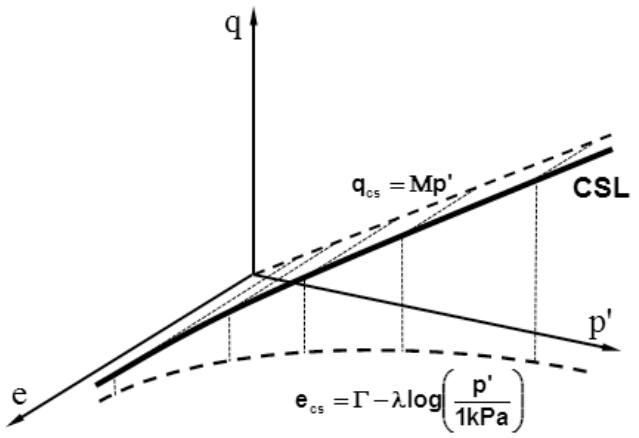

Figure 2. The sediment response is captured in the space defined by the mean effective stress p′, the deviatoric stress q, and void ratio e. The critical state line CSL is the locus of points where sediments shear at constant volume. Its projection on the p′-q plane is used to determine Coulomb strength parameters. The CSL projection on the p′-e plane defines the sediment void ratio at constant volume shear.

[13] Classical data analysis is based on two concepts in mechanics that relate shear τ and normal stress σ': (1) Mohr circle, i.e., the stress at a point in equilibrium, and (2) the Coulomb failure criterion, i.e., the linear envelope $\tau = c + \sigma' \tan\phi$ to shear strength data, where c is apparent cohesion and ϕ is the angle of internal shear strength.

[14] The complete characterization of the sediment mass must consider both the evolution in effective stress and in sediment volume. We define the "mineral void ratio" e in terms of pore volume V_v, hydrate volume V_h, and mineral volume V_m:

$$e = \frac{V_v + V_h}{V_m} \tag{1}$$

"Critical state" is reached when the specimen shears at constant void ratio. The *critical state line* CSL is the locus of critical states (i.e., points in the p′-q-e space) obtained in shear tests (Figure 2). The Coulomb strength envelope is the projection of the critical state line onto the p′-q plane; the critical state friction angle ϕ_{cs} is computed from the slope M of the critical state line on the p′-q projection as $\sin \phi_{cs} = 3M/(6 + M)$. The sediment void ratio during constant volume shear or critical state e_{cs} is a function of effective stress $e_{cs} = \Gamma - \lambda \cdot \log(p'/1\ kPa)$, where λ is the slope and Γ the intercept at 1 kPa of the critical state line projection on the e-p′ plane.

3.2. Hydrate-Free Sediments

[15] Stress-strain curves obtained during deviatoric loading for loose and dense hydrate-free sand (S_h = 0%) reveal contractive and dilative behaviors that depend on confining stress and porosity, in agreement with typical sediment behavior. The response during deviatoric loading at an initial effective confining stress σ'_o = 1 MPa is shown in Figure 3 (refer to the trend for S_h = 0%).

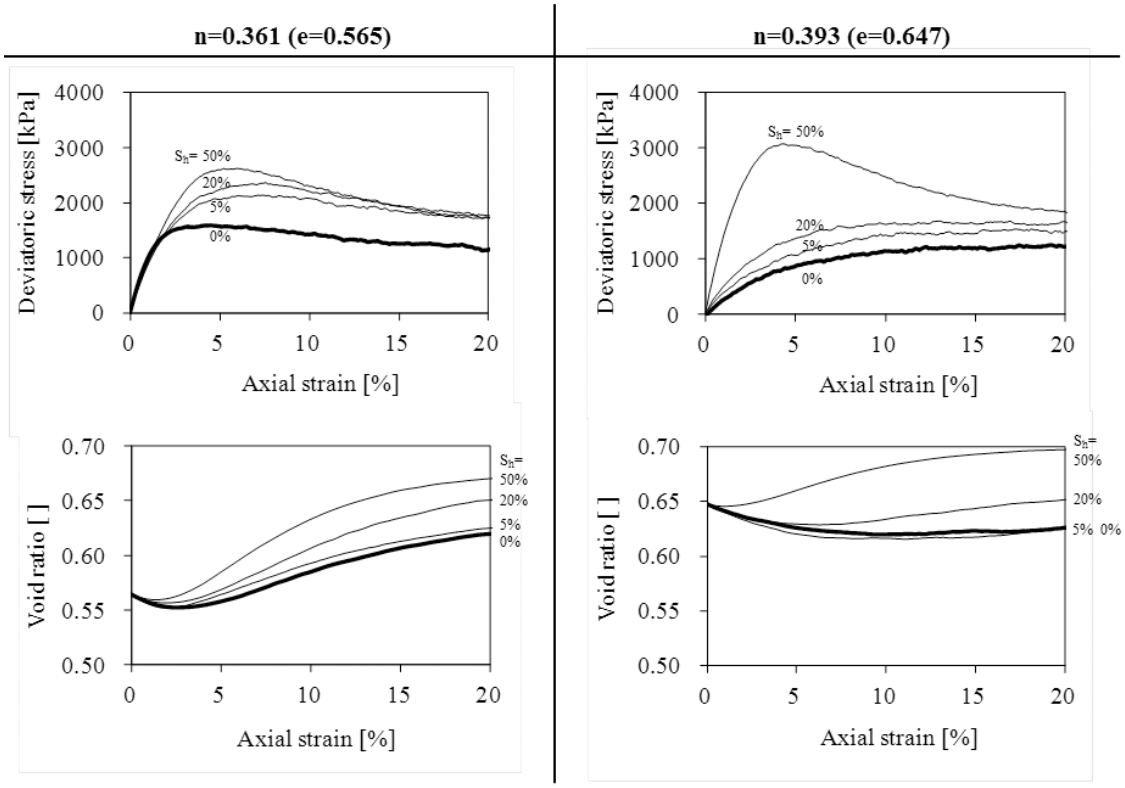

Figure 3. Distributed hydrate-bearing sediment with hydrate saturation S_h: (top) deviatoric stress and (bottom) void ratio as functions of axial strain (effective confining stress σ'_o = 1 MPa; see Figure 1b). Void ratio and shear strength approach constant volume shear critical state conditions at large strain.

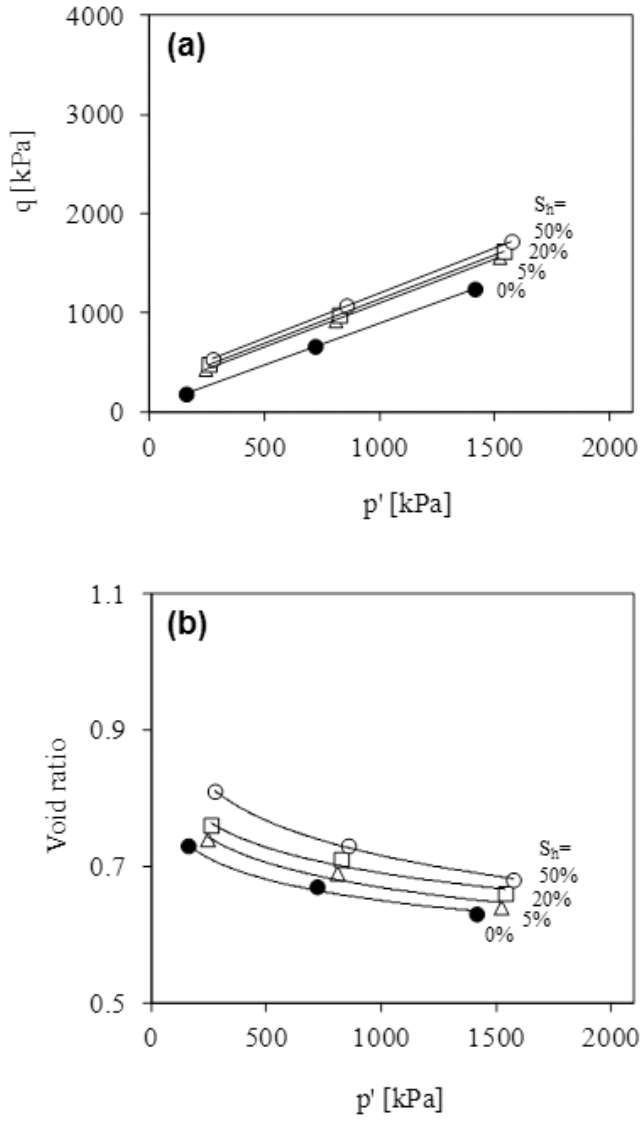

Figure 4. Critical state line CSL for distributed hydrate-bearing sediments (a) CSL projection on p′-q plane, and (b) CSL projection on e-p′ plane. Some apparent cohesion emerges with hydrate saturation (extrapolation to zero mean effective stress p′ = 0), but there is almost no effect on critical state friction angle ϕ_{cs}.

[16] The dense sand shows higher stiffness and maximum dilation near the peak strength, followed by strain softening. The void ratio e and the deviatoric stress q reach constant values at large strains, i.e., the critical state. In contrast, the loose sand shows a monotonic contractive response. Void ratio and shear strength asymptotically approach critical state conditions (note minor volume change is still observed at 20% strain in Figure 3).

[17] Numerical results are shown in Figure 4. The critical state parameters recovered for the hydrate-free sand (refer to S_h = 0% lines) are $\lambda = 0.103$, $\Gamma = 0.959$ and $\phi_{cs} = 25°$. These values fall between values for Ottawa 20–30 sand and Ottawa F110 sand. (Note Ottawa 20–30 is a uniformly graded, rounded quartzitic sand that passes through sieve 20 and is retained on sieve 30, 600 μm < d < 850 μm; its critical state parameters are $\lambda = 0.053$, $\Gamma = 0.806$ at 1 kPa, $\phi_{cs} = 28°$. Ottawa F110 sand is similar but with a median grain size of 110 μm and critical state parameters $\lambda = 0.077$, $\Gamma = 0.937$ at 1 kPa and $\phi_{cs} = 31°$; data from *Santamarina and Cho* [2001].)

3.3. Distributed Hydrate-Bearing Sands

[18] Results plotted in Figures 3 and 4 (for σ'_o = 1 MPa) show that the presence of distributed hydrate causes higher values of stiffness (particularly in the loose sand), dilative tendency (especially when $S_h \geq 20\%$), peak strength, mineral void ratio, and strength at critical state. The peak strength increases nonlinearly with hydrate saturation (Figure 3) and the critical state line shifts to higher shear strengths with increasing hydrate saturation (Figure 4a). Due to high dilation at low confinement, the Coulomb failure envelope exhibits some "apparent cohesion" when the linear trend is extrapolated to zero mean effective stress p′ = 0; there is only a minor effect on critical state friction angle ϕ_{cs} (Figure 4b).

[19] Volumetric parameters are assessed in the e-p′ projection. Critical state parameters λ and Γ are markedly affected by hydrate saturation: the presence of hydrate in the pore space hinders contraction and promotes dilation (Figure 4b).

3.4. Patchy Hydrate Saturation

[20] Sands with patchy hydrate saturation have an apparently similar global stress-strain response to that of evenly distributed hydrate-bearing sediments. However, there are two important differences. First, volume change trends resemble those of hydrate-free sediments, and hydrate-enhanced dilation is delayed compared to sediments with distributed hydrate (Figure 5; note some dilation is still taking place at 20% strain). Second, there is almost no impact on apparent cohesion because patches are surrounded by hydrate-free frictional sediment; instead, there is a significant increase in critical state friction angle, from $\phi_{cs} = 25°$ when $S_h = 0$, to $\phi_{cs} = 41°$ when $S_h = 50\%$ (Figure 6a).

4. Analyses and Discussions

4.1. Patchy Saturation

[21] The same global hydrate saturation can be obtained using a small number of large clusters or many small clusters. Implications are explored in Figure 7 where a medium with $S_h = 20\%$ is simulated with specimens that contain from 5 to 25 clusters. Results show that, at the same hydrate saturation, a higher number of smaller clusters leads to higher strength and dilative tendency (note we anticipate that the position of patches in small specimens has an important effect on the macroscale response).

4.2. Patchy Saturation Versus Distributed Hydrate

[22] Peak strengths obtained using the two different hydrate pore habits are compared in Figure 8. Results show that peak strengths in distributed hydrate-bearing sands are generally higher than in sediments with patchy hydrate saturation (S_h < 50% range): distributed hydrate, as well as a larger number of smaller clusters, force the development of more tortuous shear planes. Note that distributed hydrate can be considered the asymptotic condition for the small size

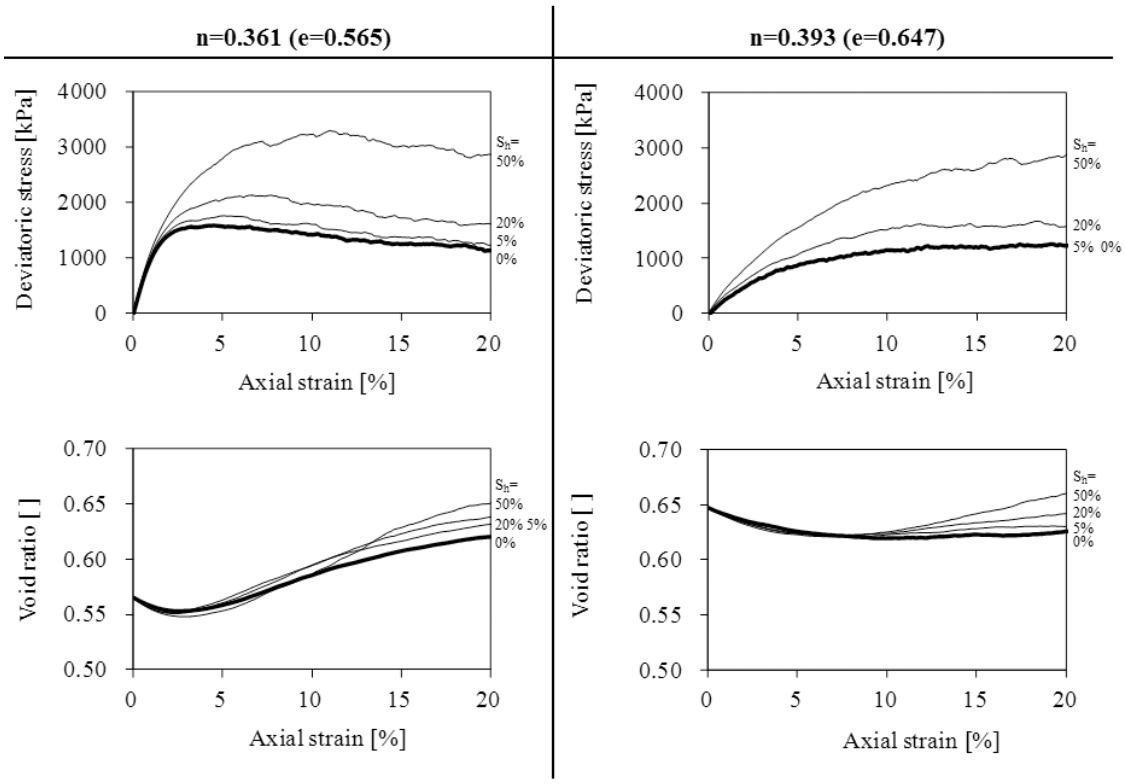

Figure 5. Sediment with patchy hydrate saturation (15 sediment clusters): (top) deviatoric stress and (bottom) void ratio as functions of axial strain (effective confining stress σ'_o = 1 MPa; see Figure 1c). Void ratio change trends resemble those of hydrate-free sediments, and hydrate-enhanced dilation is delayed compared to sediments with distributed hydrate.

clusters. Therefore, there is inherent agreement between the results in Figures 7 and 8 (applicable within the low-hydrate saturation regime, S_h < 50%).

4.3. Strength: Particle Level Mechanisms

[23] Internal particle-scale information is extracted in terms of normal contact force chains. Selected results shown in Figure 9 indicate that load transfer concentrates along stiffer hydrate-filled zones (Figures 9c and 9d; note these are 2D simulation results to facilitate visualization). Distributed hydrate particles bonded onto mineral surfaces contribute to shear resistance by bonding contiguous particles together and by promoting rotational frustration (note only mineral-to-mineral contacts are shown in Figure 9). The analysis of particle level forces in specimens with patchy hydrate saturation shows long-range interaction between clusters through the development of load-carrying columns (Figure 9d). These strong, hydrate saturated patches cause the development of tortuous rather than planar shear planes and higher energy is required to shear the specimen as compared to hydrate-free sediments, i.e., higher friction angle.

4.4. Comparison of Experimental Versus Numerical Strength Values

[24] Numerical results obtained in this study for distributed hydrate-bearing sands at various hydrate saturations, porosities, and confining stresses are compared against experimental results obtained using cementing and pore-filling hydrate distributions (Figure 10). All results show that strength increases with higher confinement, higher hydrate saturation, and lower porosity. Furthermore, in agreement with numerical simulations, experimental results show that shear strength is also affected by formation history and hydrate pore habit; in particular, hydrate-bearing sands with cementing hydrate distribution exhibit higher strength than sands with pore-filling hydrate.

4.5. Midstrain Stiffness

[25] The secant modulus E_{50} is determined for all simulations using the strain at half the peak deviatoric stress $\sigma_{dev}^{max}/2$ relative to the origin of the stress-strain curve. Results in Figure 11 show that the sediment secant stiffness E_{50} is a function of confining stress σ'_o, hydrate saturation S_h, and initial porosity n. Let us adopt an expression that combines the Hertzian stress-dependent stiffness of the granular skeleton in parallel with the stiffness contributed by the hydrate mass [*Santamarina and Ruppel*, 2010]:

$$E_{50} = a\left(\frac{\sigma'_o}{1kPa}\right)^b + cE_{hyd}(S_h)^d \quad (2)$$

where the fitting parameters represent "a" the hydrate-free sand stiffness at σ'_o = 1 kPa; "b" the sensitivity of hydrate-free sand stiffness to confining stress; "c" the contribution of the hydrate stiffness (isothermal Young's modulus E_{hyd} = 8.4 GPa [*Sloan and Koh*, 2008]) for a given pore habit, i.e., pore filling, cemented, or patchy saturation; and "d" the nonlinear effect of hydrate saturation. Factors a and

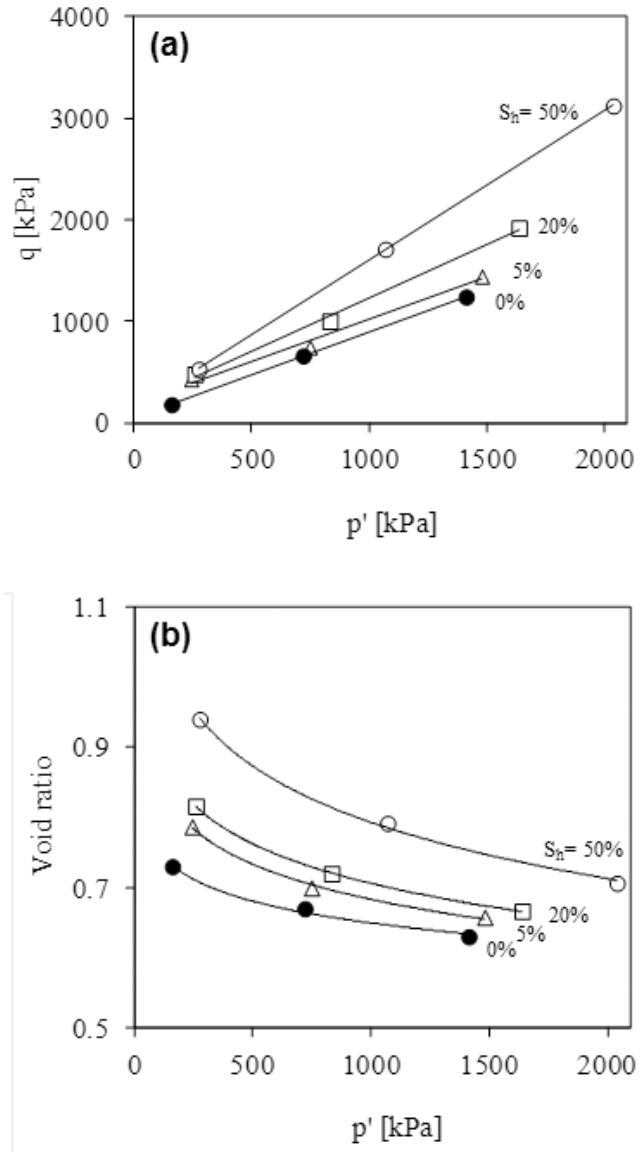

Figure 6. Critical state line CSL for sediments with patchy hydrate saturation (15 sediment clusters): (a) CSL projection on p′-q plane, and (b) CSL projection on e-p′ plane. There is almost no impact on apparent cohesion (extrapolation to zero mean effective stress p′ = 0) but a significant increase in critical state friction angle with increasing hydrate saturation.

b are extracted from simulations conducted on hydrate-free sands (n = 0.361: a = 0.41 MPa and b = 0.69; n = 0.393: a = 0.72 MPa and b = 0.50), while c and d are obtained from simulation results for the various hydrate saturations (n = 0.361: c = 0.004 and d = 0.5; n = 0.393: c ≈ 0.02 and d = 1.2). Results summarized in Figure 11 show that (1) the high stress exponent b reflects the role of fabric change on the midstrain stiffness and (2) the increase in stiffness with hydrate saturation is more pronounced in sands with high initial porosity (higher c and d values for higher sediment porosity n).

4.6. Hydrate Dissociation

[26] The impact of hydrate dissociation is investigated under the following end-member reservoir boundary conditions: (1) constant stress boundary CS, (2) zero strain boundary ZS, and (3) constant vertical stress but zero lateral strain K_o condition. The specimen with distributed hydrate S_h = 20% and confined at 1 MPa is subjected to a gradual decrease in hydrate particle size. We repeat the study at low and high deviatoric stresses.

[27] Results in Figure 12 show that the stress-strain response in sands during hydrate dissociation depends on reservoir boundary conditions and the level of deviatoric stress; in particular:

[28] 1. Hydrate dissociation in a low deviatoric stress state induces contraction without failure under constant stress boundary CS (note that the deviatoric stress when hydrate dissociates is lower than the maximum deviatoric stress the hydrate-free sediments can withstand). Conversely, the sediment fails during dissociation when the deviatoric stress is higher than the strength of the hydrate-free sediment (see analogous experimental results of *Hyodo et al.* [2008]).

[29] 2. Vertical and lateral stresses dramatically decrease during hydrate dissociation under zero strain boundary conditions ZS. In this case, an overlying rigid caprock stratum could fail in bending.

[30] 3. Vertical K_o consolidation occurs during hydrate dissociation under a constant vertical stress and zero lateral strain boundary conditions [see also *Lee et al.*, 2010]. While the sediment does not approach failure, overlying rigid layers will experience bending effects.

5. Conclusions

[31] Numerical DEM simulations provide unique insight into the mechanical response of hydrate-bearing sediments. In particular, they permits exploring formation history and various hydrate pore habits, such as recently formed distributed hydrate or in the form of patchy saturation if hydrate has been left to ripen.

[32] Simulation results obtained for hydrate-bearing sands with both distributed and patchy saturation reveal that stiffness, strength and the dilative tendency increase when the sediment density or the degree of hydrate saturation increases. Therefore, the critical state line shifts toward higher void ratios and higher strength values. The mechanical properties of hydrate-bearing sediments can be expressed as functions of hydrate saturation S_h, initial porosity n_o and effective stress σ'_o.

[33] There are differences between the mechanical properties of sands with distributed and patchy hydrate saturation. Hydrate saturation increases the apparent cohesion but has almost no effect on critical state friction ϕ_{cs} in sands with distributed hydrate. On the other hand, there is a significant increase in critical state friction angle, at null apparent cohesion, in sands with patchy saturation.

[34] In both cases, the increase in strength results from hindered particle rotation (i.e., distributed hydrate) and more tortuous failure planes (i.e., larger number of patches). Overall, the strength is slightly lower for sands with patchy hydrate saturation.

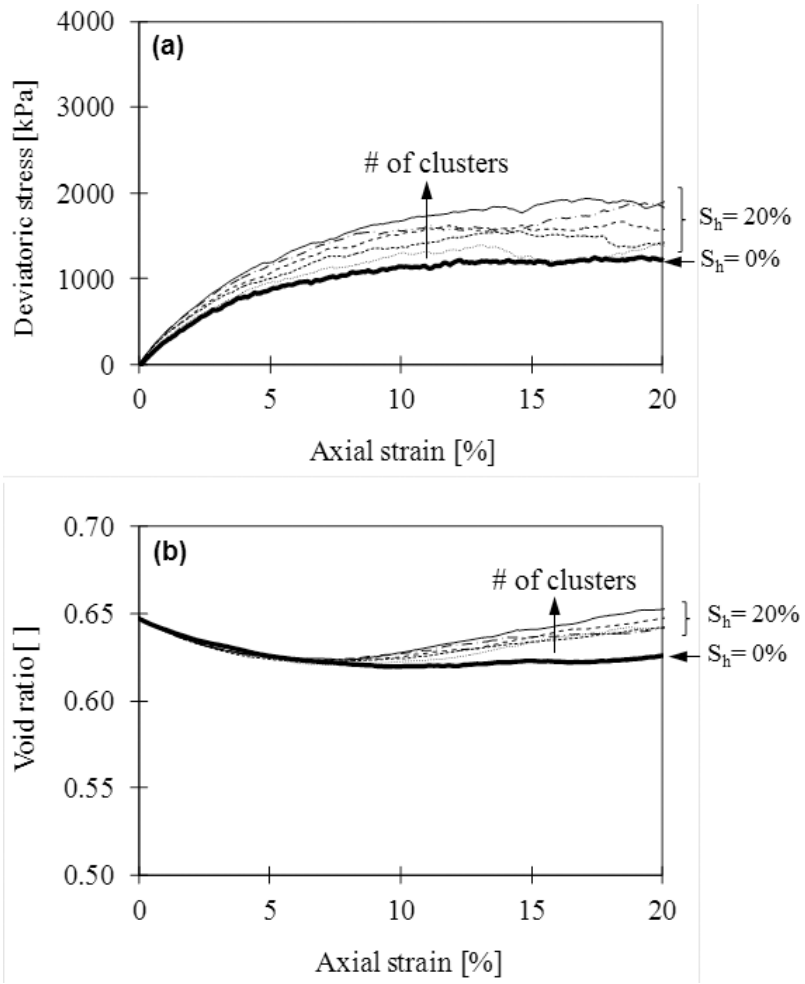

Figure 7. Sediment with patchy hydrate saturation: stress, strain, and volume change. The effect of cluster size or number of clusters at the same hydrate saturation S_h = 20%. (a) Stress-strain response. (b) Volume change. The number of clusters is 5, 10, 15, 20, and 25 in the direction of the arrow. Note effective confining stress = 1 MPa, initial porosity = 0.393. A higher number of smaller clusters leads to a higher strength and dilative tendency.

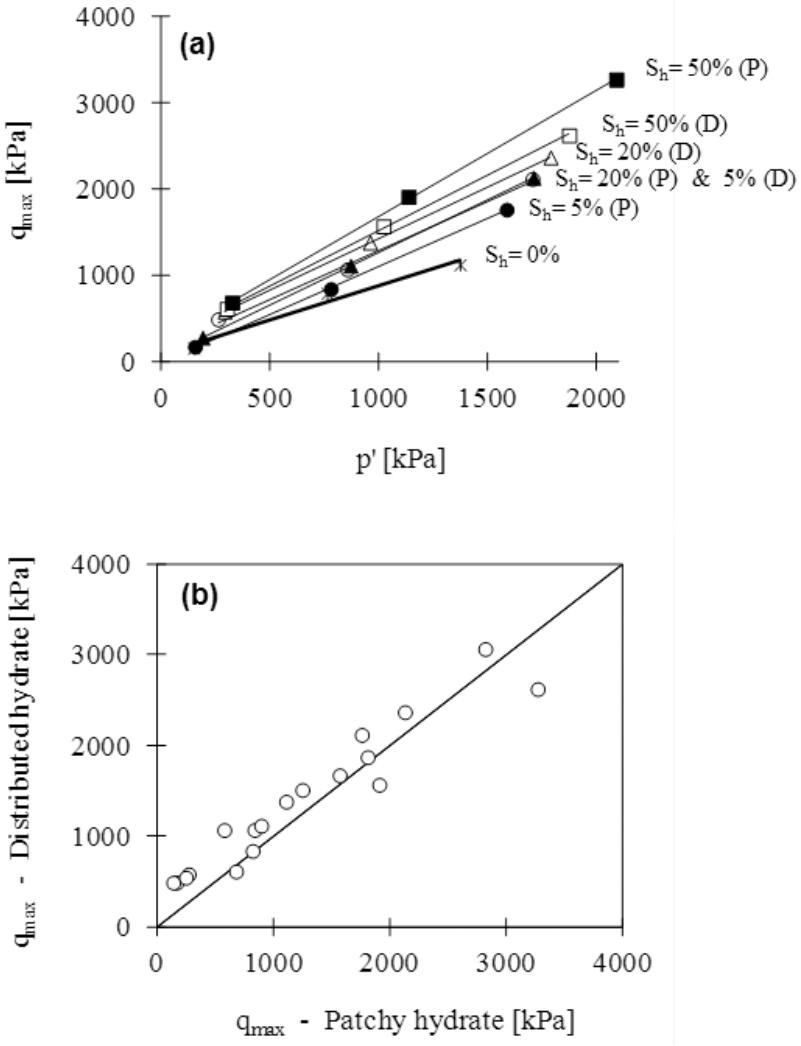

Figure 8. Peak strength q_{max} comparison between distributed hydrate-bearing sediments (open symbols) and patchy hydrate (solid symbols). (a) The p′-q plane. (b) All the data, i.e., results for two values of porosity (n = 0.361 and 0.393), three hydrate saturations (S_h = 5%, 20%, 50%), and three effective confining stress (σ'_d = 0.1 MPa, 0.5 MPa, 1 MPa). Peak strengths in distributed hydrate-bearing sands are generally higher than in sediments with patchy hydrate saturation.

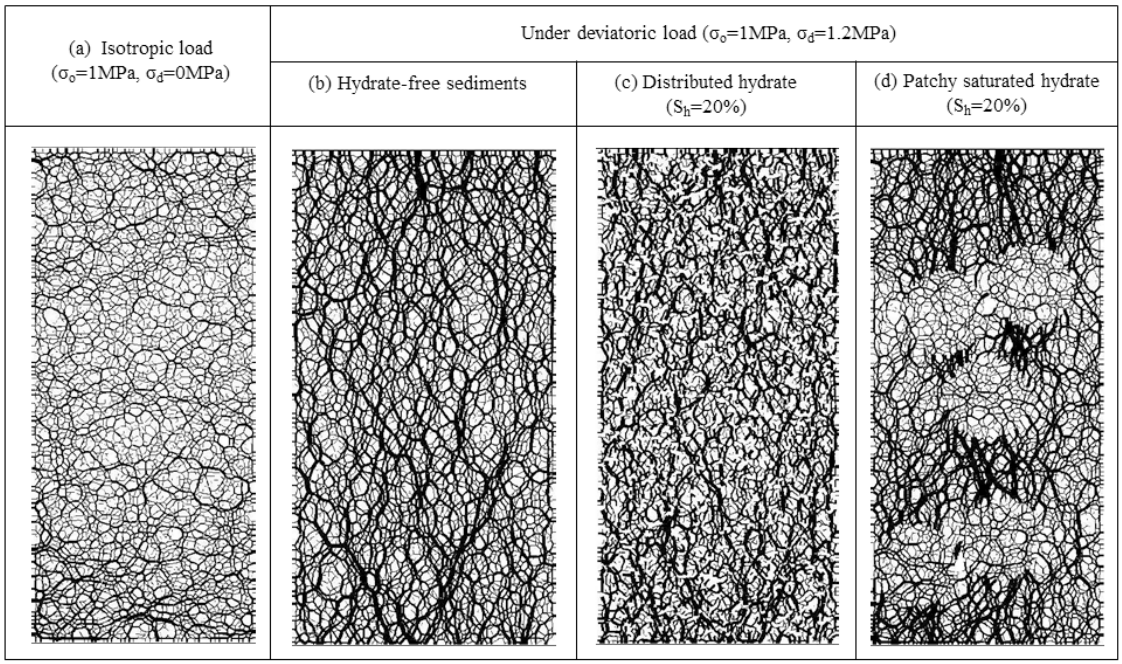

Figure 9. Normal contact force chains between mineral particles (2D simulations). Images are shown (a) after consolidation to 1 MPa of hydrate-free sediments and after an additional 1.2 MPa deviatoric stress is applied to (b) hydrate-free sediments, (c) distributed hydrate-bearing sediments, and (d) sediments with patchy hydrate saturation. Load transfer concentrates along stiffer hydrate-filled patches.

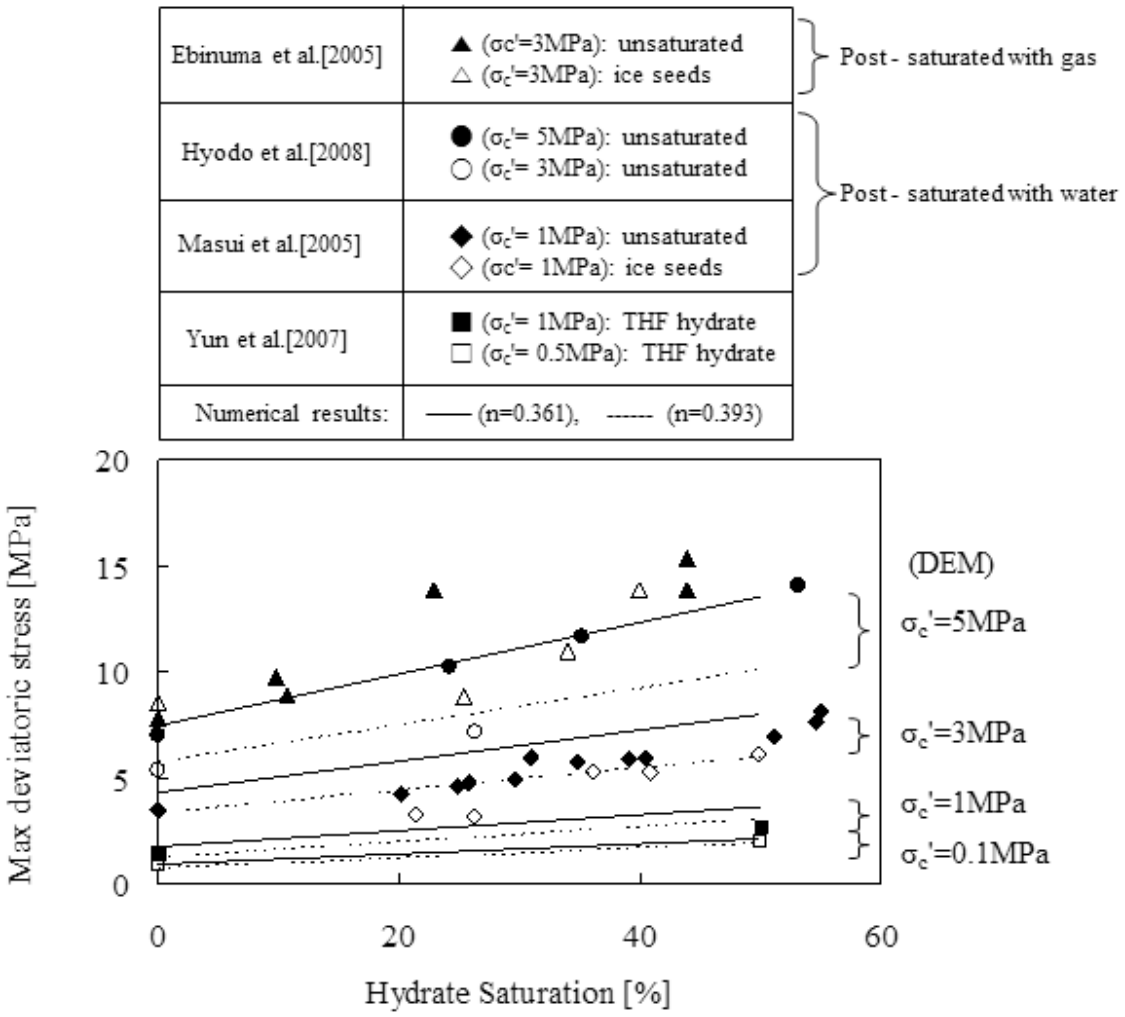

Figure 10. Strength of hydrate-bearing sediments: experimental data and DEM results (cementing hydrate, unsaturated method; pore-filling hydrate, ice seeds method). Strength increases with higher confinement, higher hydrate saturation, and lower initial porosity.

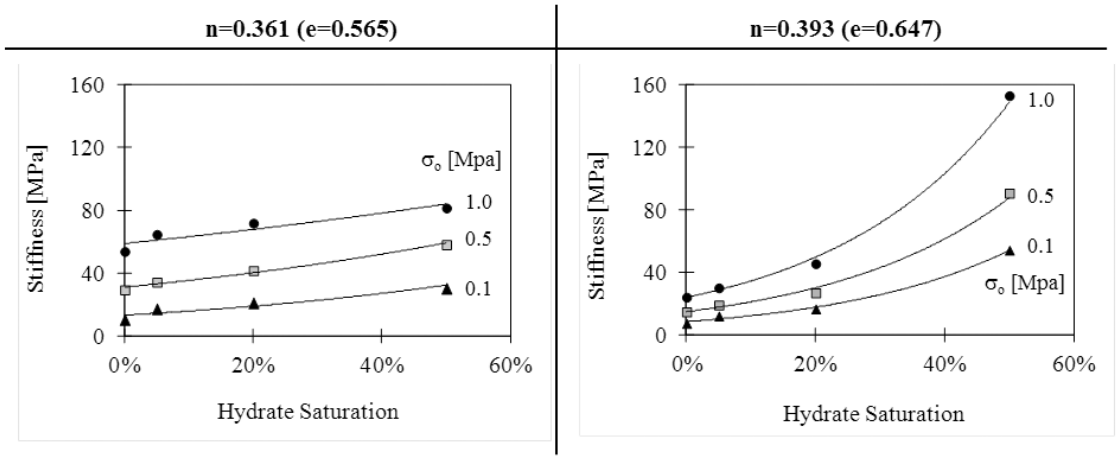

Figure 11. Midstrain stiffness of hydrate-bearing sediments (distributed hydrate) as a function of hydrate saturation and effective stress. The sediment secant stiffness E_{50} is a function of confining stress σ'_o, hydrate saturation S_h, and initial porosity n.

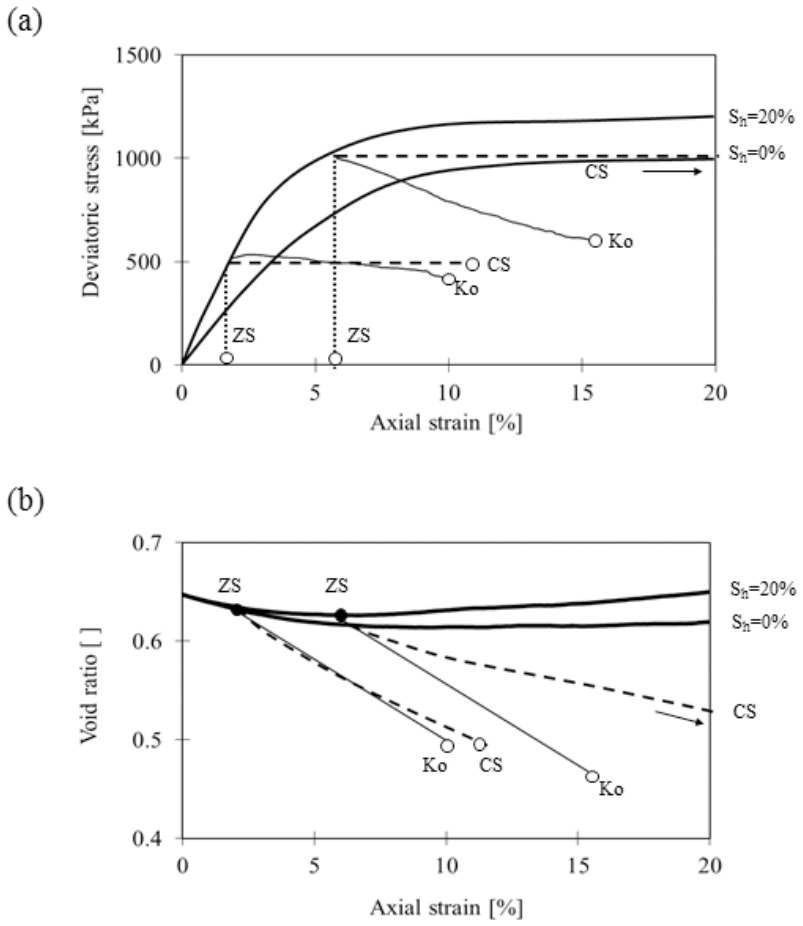

Figure 12. Hydrate dissociation under different reservoir boundary conditions (S_h = 20%, initial mean effective stress 1 MPa): (a) constant stress boundary CS: failure during hydrate dissociation depends on deviatoric stress-state before hydrate dissociation, (b) zero strain boundary ZS: vertical and lateral stresses decrease during hydrate dissociation, or (c) constant vertical stress but zero lateral strain K_o condition: the sediment vertically contracts during hydrate dissociation. Note solid heavy lines represent stress and void ratio change as functions of axial strain for 0% and 20% hydrate saturation.

[35] Particle-scale contact force data show the concentration of load transfer along hydrate-stabilized stiffer granular chains and stiff regions such as patches.

[36] Complementary numerical simulation results show that hydrate dissociation under different reservoir boundary conditions causes volume contraction and/or stress relaxation. Pronounced shear strains develop if the hydrate-bearing sediment is subjected to deviatoric loading during dissociation.

[37] **Acknowledgments.** Support for this research was provided by the U.S. Department of Energy. Additional funding was provided by the Goizueta Foundation.

References

Ebinuma, T., Y. Kamata, H. Minagawa, R. Ohmura, J. Nagao, and H. Narita (2005), Mechanical properties of sandy sediment containing methane hydrate, in *Proceedings of the Fifth International Conference on Gas Hydrates*, pp. 958–961, Tapir Acad., Trondheim, Norway.

Hyodo, M., Y. Nakata, N. Yoshimoto, and J. Yoneda (2008), Shear strength of methane hydrate bearing sand and its deformation during dissociation of methane hydrate, in *Deformation Characteristics of Geomaterials*, pp. 549–556, IOS, Amsterdam.

Jung, J. W., and J. C. Santamarina (2011), Hydrate adhesive and tensile strengths, *Geochem. Geophys. Geosyst.*, *12*, Q08003, doi:10.1029/2010GC003495.

Klar, A., K. Soga, and M. Y. A. Ng (2010), Coupled deformation-flow analysis for methane hydrate extraction, *Geotechnique*, *60*(10), 765–776.

Lee, J. Y., J. C. Santamarina, and C. Ruppel (2010), Volume change associated with formation and dissociation of hydrate in sediment, *Geochem. Geophys. Geosyst.*, *11*, Q03007, doi:10.1029/2009GC002667.

Masui, A., H. Haneda, Y. Ogata, and K. Aoki (2005a), Effect of methane hydrate formation on shear strength of synthetic methane hydrate sediments, in *Proceedings of the Fifteenth (2005) International Offshore and Polar Engineering Conference*, pp. 364–369, Int. Soc. of Offshore Polar Eng., Cupertino, Calif.

Masui, A., H. Haneda, Y. Ogata, and K. Aoki (2005b), The effect of saturation degree of methane hydrates on the shear strength of synthetic methane hydrate sediments, in *Proceedings of the Fifth International Conference on Gas Hydrates*, pp. 657–663, Tapir Acad., Trondheim, Norway.

Moridis, G. J., et al. (2011), Challenges, uncertainties, and issues facing gas production from gas-hydrate deposits, *SPE Reservoir Eval. Eng.*, *14*(1), 76–112, doi:10.2118/131792-PA.

Nixon, M. F., and J. L. H. Grozic (2007), Submarine slope failure due to gas hydrate dissociation: A preliminary quantification, *Can. Geotech. J.*, *44*, 314–325.

Ohmura, R., T. Shigetomi, and Y. H. Mori (2002), Bending tests on clathrate hydrate single crystals, *Philos. Mag. A*, *82*(9), 1725–1740.

Rutqvist, J., and G. J. Moridis (2009), Numerical studies of geomechanical stability of hydrate-bearing sediments, *SPE J.*, *14*(2), 267–282, doi:10.2118/126129-PA.

Santamarina, J. C., and G. C. Cho (2001), Determination of critical state parameters in sandy soils—Simple procedure, *Geotech. Test. J.*, *24*(2), 185–192.

Santamarina, J. C., and C. Ruppel (2010), The impact of hydrate saturation on the mechanical, electrical, and thermal properties of hydrate-bearing sand, silts, and clay, in *Geophysical Characterization of Gas Hydrates*, *Geophys. Dev. Ser.*, vol. 14, edited by M. Riedel, C. Willoughby, and S. Chopra, pp. 373–384, Soc. of Explor. Geophys., Tulsa, Okla.

Sloan, E. D., and C. A. Koh (2008), *Clathrate Hydrates of Natural Gases*, 3rd ed., CRC Press, Boca Raton, Fla.

Soga, K., S. L. Lee, M. Y. A. Ng, and A. Klar (2006), Characterisation and engineering properties of methane hydrate soils, in *Characterisation and Engineering Properties of Natural Soils*, edited by T. S. Tan et al., pp. 2591–2642, A. A. Balkema, Lisse, Netherlands.

Waite, W. F., et al. (2009), Physical properties of hydrate-bearing sediments, *Rev. Geophys.*, *47*, RG4003, doi:10.1029/2008RG000279.

Wang, Y.-H., and S.-C. Leung (2008), A particulate-scale investigation of cemented sand behavior, *Can. Geotech. J.*, *45*, 29–44.

Yun, T. S., J. C. Santamarina, and C. Ruppel (2007), Mechanical properties of sand, silt, and clay containing tetrahydrofuran hydrate, *J. Geophys. Res.*, *112*, B04106, doi:10.1029/2006JB004484.

J.-W. Jung, Lawrence Berkeley National Laboratory, 1 Cyclotron Rd., Berkeley, CA 94720, USA. (jwjung7695@gmail.com)

J. C. Santamarina, School of Civil and Environmental Engineering, Georgia Institute of Technology, Atlanta, GA 30332, USA.

K. Soga, Department of Engineering, University of Cambridge, Cambridge CB2 1TN, UK.